RSC Advances

PAPER

View Article Online
View Journal | View Issue

Cite this: *RSC Adv.*, 2025, **15**, 26082

Preparation of graphene oxide based on microcrystalline graphite: the study of microwave absorption properties

Yunsheng Zheng,[a] Zhijun Ma, *[ab] Xingyuan Weng,[a] Liang Cheng[a] and Ying Qin[a]

Electromagnetic wave absorption materials play an increasingly important role in modern society for military stealth technology and 5G smart era. Microcrystalline graphene oxide (MGO) absorption materials have prepared by chemical oxidation method using microcrystalline graphite as raw material. The lamellar structure, functional groups, defects, and microwave absorption properties of MGO have characterized by X-ray diffractometer (XRD), Raman Spectrometer (Raman), Fourier Transform Infrared Spectrometer (FT-IR), Atomic Force Microscope (AFM), and Vector Network Analyzer (VNA). It is elucidated that the electromagnetic wave absorption mechanism of MGO. The results show that when the dosage of microcrystalline graphite is 1.0 g, the overall layer number of the MGO-1.0 is 1–2 layers, layer spacing is 0.900 nm, which exhibits the best microwave absorption properties, with its minimum reflection loss (RL_{min}) reaching −18.39 dB and its effective absorption band (EAB) is 3.06 GHz (7.97–11.03 GHz) at the microwave absorption layer thickness of 3.6 mm and the frequency of 9.42 GHz. This excellent microwave absorption properties is attributed to dipole polarization, defect polarization, and conductive loss. It is worth noting that the high conductivity, polar group, and edge defect density will cause the impedance mismatch of MGO and affect the microwave absorption properties.

Received 30th March 2025
Accepted 4th July 2025

DOI: 10.1039/d5ra02203g

rsc.li/rsc-advances

1 Introduction

In the context of the rapid development of information communication and artificial intelligence, the application of electromagnetic wave in communication and detection occupies a dominant position and promotes the rapid development of human civilization.[1–3] However, electromagnetic pollution can not be ignored. In view of the potential harm of electromagnetic wave in the field of human health and national defence, it is of great significance to develop and design high-performance microwave absorption materials (MAMs).[4,5] However, traditional MAMs has certain limitations in application due to its characteristics.[6] Metal materials usually have high conductivity, but the impedance matching is poor, and the electromagnetic wave loss mechanism is single. Ceramic-based MAMs has good corrosion resistance, high mechanical strength, and a rich microwave loss mechanism, but it has some disadvantages such as high density and complex production process. Ferrite has good microwave absorption properties and absorption bandwidth, but there are problems such as large matching thickness and poor corrosion resistance.[7] However, graphene oxide (GO) has been fevered by researchers due to its advantages of lightweight, high conductivity, large specific surface area, and strong dielectric loss, and is considered to be a highly competitive high-performance MAMs.[8–10]

According to the different degrees of graphite crystallization, it can be divided into crystalline graphite and microcrystalline graphite two categories. At present, crystalline graphite is the main raw material for the preparation of graphene. Ma[11] used flake graphite as raw material to prepare graphene with layer spacing of 0.91 nm by using improved Hummers' method. The RL_{min} at 17.83 GHz reached −34.28 dB, and the microwave absorption properties was excellent. Compared with flake graphite, microcrystalline graphite has a high grade and easy development, with an average carbon content of 60–80%. Because of its unique characteristics, it has attracted much attention from researchers. Xie[12,13] found that microcrystalline graphite can be used as MAMs by studying the composite of microcrystalline graphite and low-density polyethylene material. Graphene is the product of graphite after chemical oxidation and stripping. With the oxidation process, the defects and oxygen-containing functional groups can cause dielectric loss mechanisms such as defect polarization and dipole polarization, and improve the microwave absorption properties. Therefore, it is of great significance to study and design microcrystalline graphite to prepare graphene oxide microwave absorption materials.

At present, there are few reports about the preparation of graphene oxide microwave absorption materials using

[a]*College of Mining, Liaoning Technical University, Fuxin 123000, China. E-mail: zhijunma0930@126.com; Tel: +86-139-4188-1359*

[b]*College of Materials Science & Engineering, Liaoning Technical University, Fuxin 123000, China*

microcrystalline graphite as raw material. In this study, microcrystalline graphite has been oxidized and stripped by chemical method, and the response mechanism of MGO to dielectric loss properties of materials was studied.

2 Materials and methods

2.1 Materials

Microcrystalline graphite powder (MG), concentrated sulfuric acid (H_2SO_4, AR), potassium permanganate (K_2MnO_4, AR), concentrated hydrochloric acid (HCl, w_t = 36–38%), hydrogen peroxide (H_2O_2, w_t = 30%), and deionized water (produce in the laboratory).

2.2 Methods

2.2.1 Preparation of microcrystalline graphene oxide. Preparation of MGO using the Hummers' method[14] without the addition of $NaNO_3$. Firstly, 0.8 g, 1.0 g, 1.2 g, 1.4 g, and 1.6 g microcrystalline graphite powder are added into a three-neck flask containing 46 mL H_2SO_4, and the water bath temperature is controlled to be <10 °C and the reaction is stirred for 1 h at a rotating speed of 180 rpm. Then, add 6 g K_2MnO_4 for low temperature reaction in an ice bath of 2 h. Afterward, the temperature is raised to 35 °C for an medium temperature reaction of 6 h. Finally, slowly add 92 mL of deionized water and continue the reaction for 15 min. Slowly add 180 mL deionized water, and continue to drop 30% H_2O_2 until the reaction solution turns bright yellow, and reacts for 15 min. The reaction product is washed with 5% HCl and deionized water to neutralize. After ultrasonic peeling for 1 h, the samples of GO (MGO-0.8, MGO-1.0, MGO-1.2, MGO-1.4, and MGO-1.6) are obtained (Fig. 1).

2.2.2 Sample characterization. X-Ray Diffractometer (XRD, D8 ADVANCE, Bruker, Germany) is used to determine the phase structure of the samples under the following test conditions: Cu targeted K α-ray, 1.5406 Å wavelength, 40 kV working voltage, 40 mA tube current, 0.05 s step length, and 5–60° scanning range. The crystal plane spacing is calculated according to Bragg's formula (eqn (1)).[15]

$$d = \frac{\lambda}{2\ \sin\ \theta}\left(h^2 + k^2 + l^2\right)^{1/2} \quad (1)$$

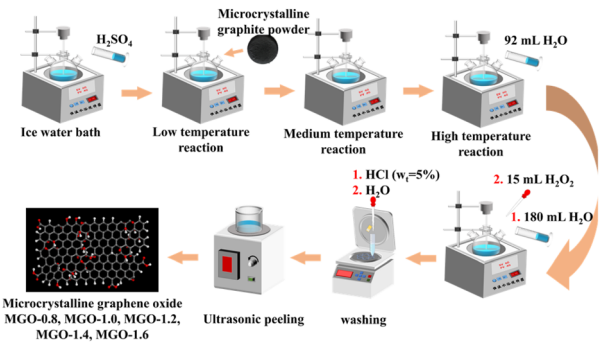

Fig. 1 Schematic illustration of the synthetic route MGO.

where, d is the crystal face spacing, nm; λ = 0.154056 nm; θ is the diffraction angle; h, k, and l are crystal face indices.

Fourier Transforms Infrared Spectroscopy (FT-IR, Tensor II, Bruker, Germany) is used to determine the chemical bonds and groups of the samples under the following test conditions: wave number range of 400–4000 cm^{-1}, the number of scans is 16 times; Raman Spectra (Raman, LabRAM HR, Horiba, Japan) is used to measure the disorder and defect density under the following test conditions: the number of test points is 3; Atomic Force Microscope (AFM, Dimension icon, Bruker, Germany) is used to determine the layer thickness under the following test conditions: the number of test points is 2, and then the number of layers of MGO is calculated.

2.2.3. Microwave absorption properties test. Vector Network Analyzer (VNA, HP8722ES, HP, America) is used to test the electromagnetic parameters (μ_r, ε_r) of the samples. The coaxial line testing method determines the complex permittivity and complex permeability of the samples in the frequency range of 1–18 GHz. The ratio of sample to paraffin wax is 5 : 5 and pressed into concentric rings with an inner diameter of 3 mm, outer diameter of 7 mm, and thickness of 2 mm. Then, from the electromagnetic parameter values calculate the RL and study the microwave absorption properties.

3 Results and discussion

3.1 Structure analysis

Fig. 2 shows XRD characterizations of MGO (Fig. 2a) and Raman characterizations of MGO (Fig. 2b).

In the XRD pattern (Fig. 2a), the characteristic diffraction peak at 2θ = 26.5947° is attributed to microcrystalline graphite, corresponding to the interlayer distance $d_{[002]}$ = 0.333 nm.[16,17] The comparison of XRD patterns shows that the characteristic diffraction peaks of MGO-0.8, MGO-1.0, MGO-1.2, MGO-1.4, and MGO-1.6 appear at 2θ = 9.5111°, 2θ = 9.8173°, 2θ = 10.1439°, 2θ = 10.1439°, and 2θ = 10.0622°. According to the Bragg equation,[18] the interlayer distances $d_{[001]}$ are 0.929 nm, 0.900 nm, 0.871 nm, 0.871 nm, and 0.878 nm, respectively, and the oxidation of microcrystalline graphite is realized. Among them, the MGO-0.8 has the largest interlayer distance, reaching 0.929 nm, and the increase in interlayer distance is due to the greater number of oxygen-containing functional groups compared with other samples.[19] In addition, due to the hydrophilic properties of MGO, there are a small number of water molecules between the interlayer graphite.

Fig. 2b shows the Raman spectra of MGO samples under different microcrystalline graphite dosing conditions. The G-peak appears near 1581 cm^{-1}, which is attributed to the in-plane vibration of sp^2 carbon atoms. For containing defects, the defect D-peak appears near 1351 cm^{-1}, which is attributed to the sp^3 hybrid orbital of carbon atoms. At the same time, D′-peak appears near 1518 cm^{-1}.[20] By using origin 2.0, the peak values of D-peak, G-peak, and D′-peak are fitted. The fitting results show that the D-peak strength (I_D = 7065.34–8344.11) is higher than that G-peak strength (I_G = 5618.14–6462.16), indicating that the oxidation process leads to structural defects and chaos. The ratio of D-peak to G-peak intensity (I_D/I_G) in carbon

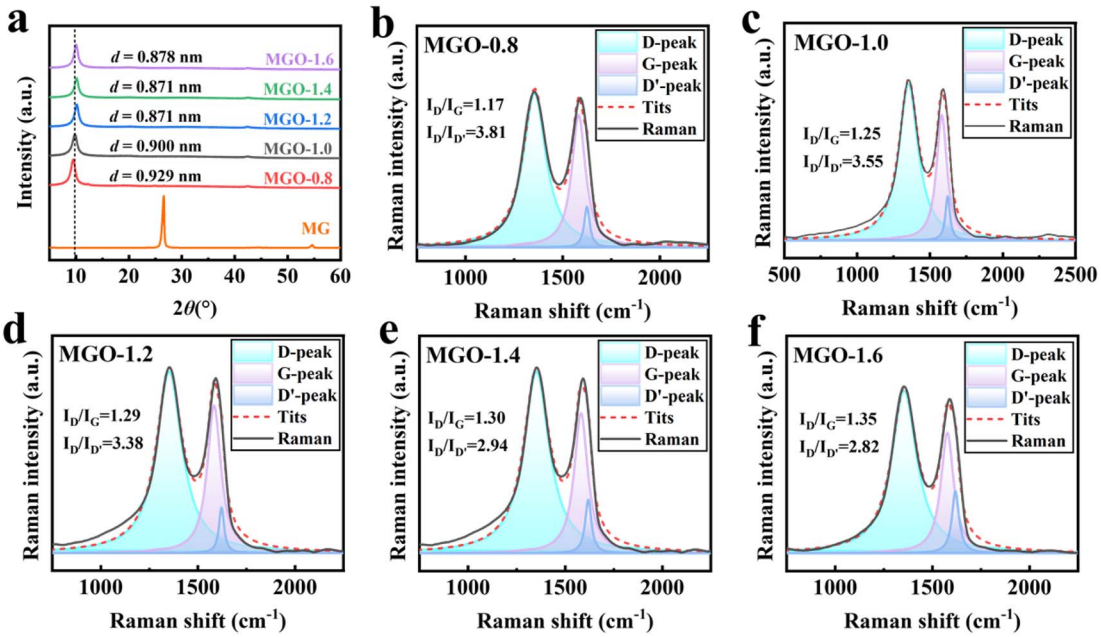

Fig. 2 Structural analysis of MGO (a – XRD of MGO; b–f – Raman of MGO).

materials is usually used as an important parameter to characterize the defect density (n_D, cm^{-2}), and the equation is $n_D = (7.3 \pm 2.2) \times 10^9 E_L^4 \left(\frac{I_D}{I_G}\right)$. And the ratio of D-peak to D′-peak intensity ($I_D/I_{D'}$) is usually used to characterize the defect types.[21] The I_D/I_G of MGO are 1.17, 1.25, 1.29, 1.30, and 1.35, and the $I_D/I_{D'}$ of MGO are 3.81, 3.55, 3.38, 2.82, and 2.94. The value range of I_D/I_G is 1.17–1.35, indicating that microcrystalline graphite was successfully oxidized and a large number of defects were produced. The value range of $I_D/I_{D'}$ is 3.81–2.82, and the value is around 3.5, indicating that the edge-type defects are dominant,[22] which is closely related to the small lamellar size and low crystallization degree of microcrystalline graphite.

3.2 Functional groups analysis

Fig. 3 shows that the FT-IR of MGO under different microcrystalline graphite dosing conditions, and the peaks fitting of FT-IR are also carried out. The peaks near 864 cm^{-1} and 974 cm^{-1} are attributed to the deformation vibration of C–H, the peaks near 1037 cm^{-1} and 1294 cm^{-1} are attributed to

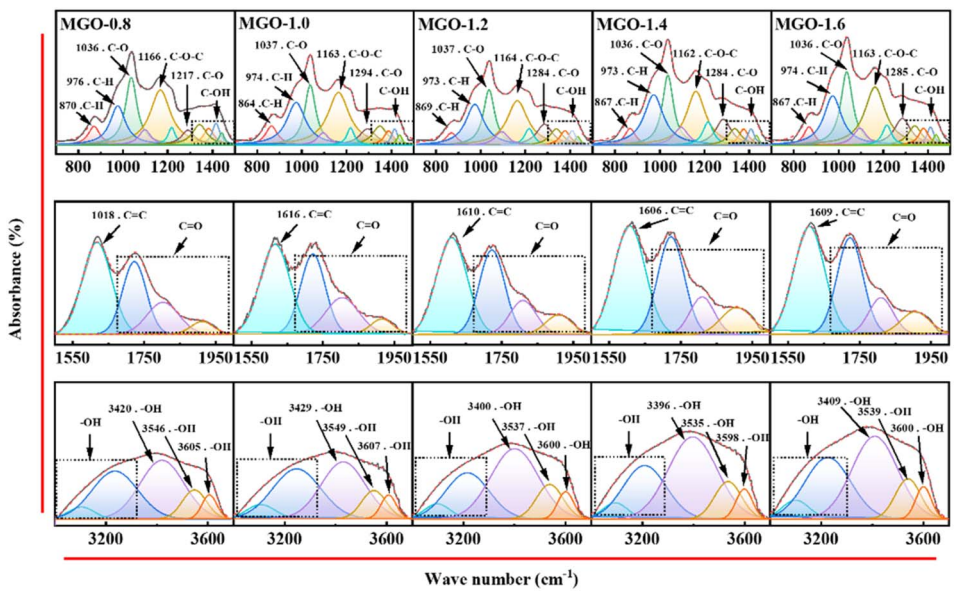

Fig. 3 Functional groups analysis of MGO.

Table 1 FT-IR semi-quantitative analysis of MGO

Sample	w_{C-H} (%)	w_{C-O} (%)	w_{C-O-C} (%)	w_{-OH} (%)	$w_{C=C}$ (%)	$w_{C=O}$ (%)
MGO-0.8	12.56	12.17	15.64	39.78	8.64	11.21
MGO-1.0	13.36	12.54	14.70	39.25	8.72	11.42
MGO-1.2	11.63	12.87	11.92	42.33	9.59	11.67
MGO-1.4	13.11	13.69	11.63	39.24	9.75	12.57
MGO-1.6	11.37	14.27	12.55	41.18	9.23	11.40

stretching vibration of C–O, the peaks near 1163 cm^{-1} is attributed to stretching vibration of C–O–C, The peaks near 1348–1437 cm^{-1} and 3107–3607 cm^{-1} are attributed to stretching vibration of –OH, the peaks near 1616 cm^{-1} are attributed to stretching vibration of C=C, and the peaks near 1721–1914 cm^{-1} are attributed to stretching vibration of C=O. The presence of these bonds between carbon and oxygen atoms attests to the full oxidation of the materials, forming hydroxyl and carboxyl groups, as well as epoxy groups with higher binding energy.

The FT-IR of MGO have been analysed by origin 2.0, and the functional group semi-quantitative analysis is performed according to the integrated area. The analysis results are shown in Table 1.

Table 1 shows the functional group content and parameters in FT-IR of MGO. The main functional group of MGO is the hydroxyl group, the content of which is 39.24–42.33%. The absorption peak of C=C is attributed to the unoxidized sp^2 hybridization in the microcrystalline graphite lattice. With the increase of microcrystalline graphite addition, the content of $w_{C=C}$ increases from 8.64% of MGO-0.8 to 9.75% of MGO-1.6, indicating that MGO-0.8 has the highest oxidation degree. In this case, more carbon atoms in the MGO-0.8 structure layer are converted from sp^2 hybridization to sp^3 hybridization, which combine with oxygen or hydroxyl groups to form C–O–C(w_{C-O-C} = 15.64%) and partial C–OH. Combined with Raman analysis (Fig. 2b), the main defect type of MGO is edge defect, with more sp^3 hybridization. In addition, there are chemical bond breaks at the edges of the microcrystalline graphite lattice. Therefore, the carbon atoms distributed at the edge of the structural layer combine with oxygen and hydroxylation to form –C=O, –COOH, and more C–OH. In summary, the FT-IR shows that a large number of oxygen-containing functional groups are introduced into the microcrystalline graphite structure, which realizes the oxidation of microcrystalline graphite.

3.3 Lamellar morphology analysis of MGO

The lamellar thickness of representative sample MGO-1.0 is further analyzed. The AFM of the MGO-1.0 is shown in Fig. 4a and b corresponding to two regions of MGO-1.0, respectively. The thickness of the two regions is 1.315 nm and 1.071 nm, respectively. Each microcrystalline graphite layer is connected by van der Waals force, and the layer spacing is 0.335 nm.[23] After oxidation, the layer spacing of MGO-1.0 is 0.900 nm (Fig. 2a), and the number of layers of the sample prepared is 1–2 layers by calculation, and the preparation of MGO is realized. In addition, there is a depression of about 0.1 nm in the middle of the same plane in Fig. 4a and b, indicating that the MGO-1.0 has more edge defects, leading to larger layer spacing, which is consistent with the Raman (Fig. 2c).

3.4 Microwave absorption properties analysis

The electromagnetic parameters (μ_r, ε_r) of MGO are measured by VNA, and the input impedance (Z_{in}, eqn (2)) and reflection loss (RL, eqn (3)) of the MGO are calculated according to the transmission line theory.[9] The electromagnetic wave absorbing capacity of MGO is evaluated by RL.

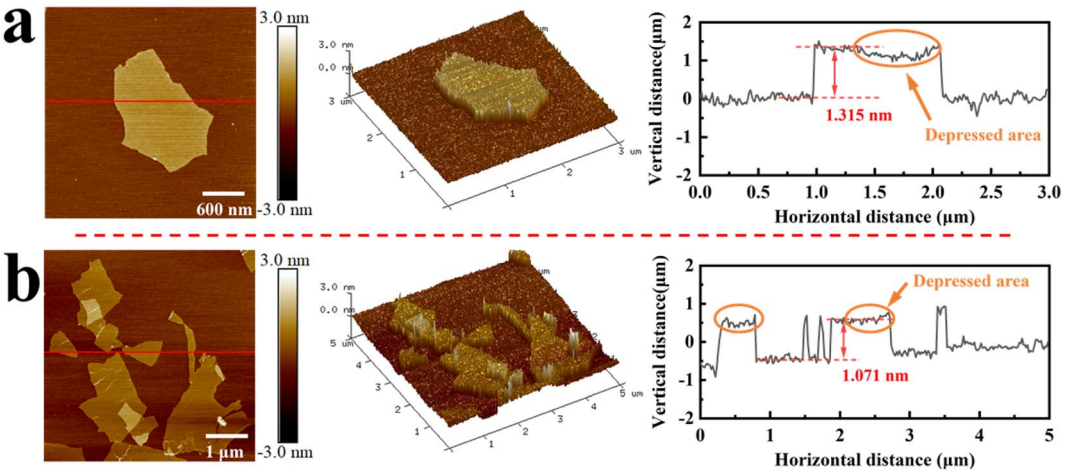

Fig. 4 AFM analysis of MGO-1.0 (a and b — corresponding to two regions of MGO-1.0).

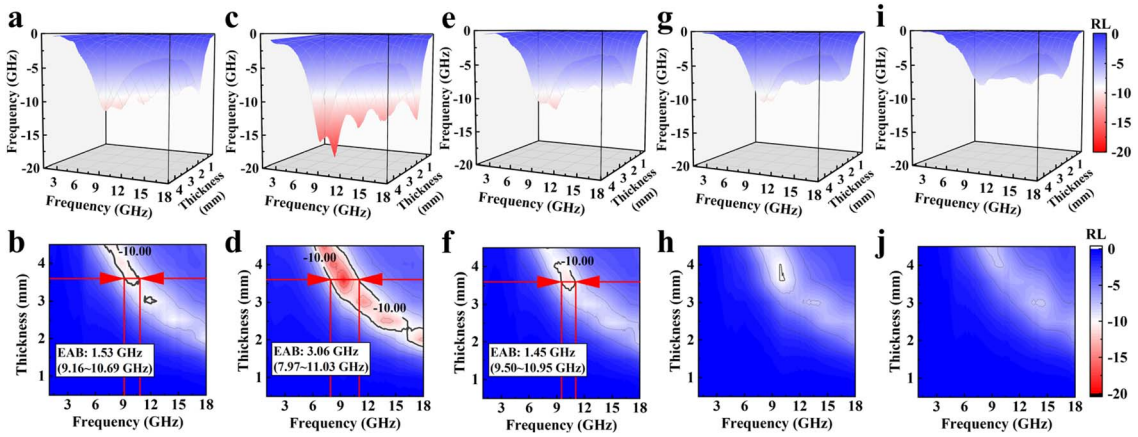

Fig. 5 The RL_{min} values of MGO under different absorbent layer thicknesses (a and b – MGO-0.8; c and d – MGO-1.0; e and f – MGO-1.2; g and h – MGO-1.4; i and j – MGO-16).

$$Z_{in} = Z_0\sqrt{\frac{\mu_r}{\varepsilon_r}}\tanh\left[j\frac{2\pi fd}{c}\sqrt{\mu_r\varepsilon_r}\right], Z_0 = \sqrt{\frac{\mu_0}{\varepsilon_0}} \quad (2)$$

$$RL = 20\lg\left|\frac{Z_{in} - Z_0}{Z_{in} + Z_0}\right| \quad (3)$$

where Z_0 is free space impedance, 376.73 Ω; d is absorption layer thickness, mm; c is electromagnetic wave propagation speed in free space, 3.0×10^8 m s^{-1}. Where, RL < −10 dB, the microwave absorption efficiency is >90%, and the corresponding frequency range is EAB.[24]

Fig. 5 shows the RL value of MGO under different absorption layer thicknesses. The RL_{min} of the MGO-0.8 is −11.16 dB at the thickness of the absorption layer of 3.6 mm and the frequency of 10.01 GHz, and the EAB is 1.53 GHz (9.16–10.69). The RL_{min} of the MGO-1.0 is −18.39 dB at the thickness of the absorption layer of 3.6 mm and the frequency of 9.42 GHz, and the EAB is 3.06 GHz (7.97–11.03 GHz). With the increase of microcrystalline graphite dosage, the electromagnetic wave absorption ability of the sample decreases. The RL_{min} of the MGO-1.2 is −11.56 dB at the absorption layer thickness of 3.6 mm and the frequency of 10.35 GHz, and the EAB is 1.45 GHz (9.50–10.95 GHz). In Fig. 5c and d, it can be found that RL_{min} can be located in the whole frequency range by adjusting the absorbent layer thickness of the samples.

3.5 Electromagnetic wave absorption mechanism analysis

To investigate more deeply the intrinsic mechanism of electromagnetic wave absorption in MGO, the complex permittivity ($\varepsilon_r = \varepsilon' - j\varepsilon''$) and the complex permeability ($\mu_r = \mu' - j\mu''$) in the range of 1–18 GHz have been analyzed. With their real and imaginary parts representing the storage and loss capacity of electromagnetic energy, respectively.[25] The loss factor ($\tan\delta_\varepsilon$, $\tan\delta_\mu$) can be represented by following eqn (4) and (5).[26,27]

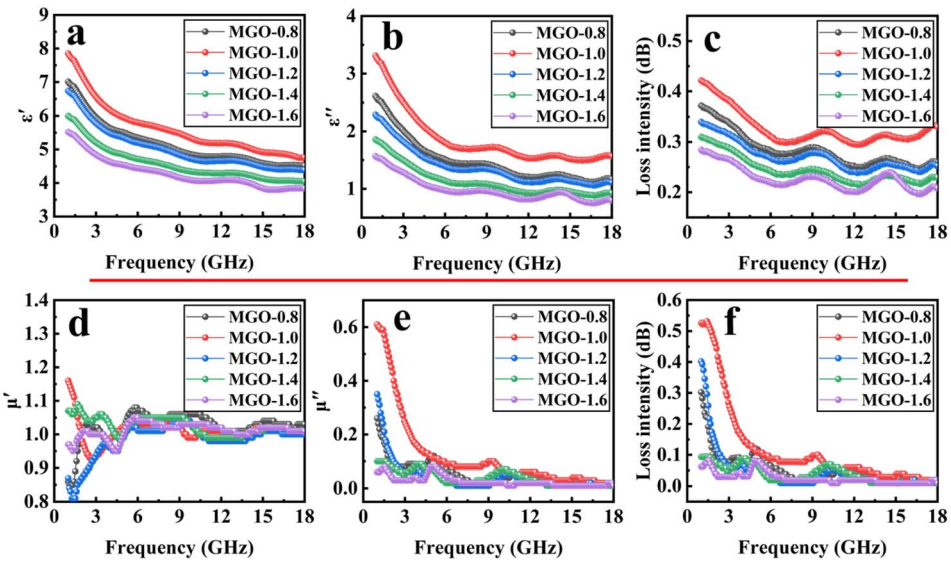

Fig. 6 Electromagnetic parameter analysis (a and b – complex permittivity real part, imaginary part, c – dielectric loss tangent value, d and e – permeability real part, imaginary part, f – magnetic loss tangent value).

$$\tan \delta_{\varepsilon} = \frac{\varepsilon''}{\varepsilon'} \quad (4)$$

$$\tan \delta_{\mu} = \frac{\mu''}{\mu'} \quad (5)$$

Fig. 6 shows the electromagnetic parameters of the MGO, where ε', ε'' is complex permittivity real parts and complex permittivity imaginary parts, μ', μ'' is complex permeability real parts and complex permeability imaginary parts. The electromagnetic parameters of all samples were obtained in the frequency range of 1–18 GHz. Both the ε' and ε'' decrease with increasing frequency, attributing to the dielectric relaxation.[28] In Fig. 6c and f, the peak of 7.97–11.03 GHz appear, indicating that MGO have strong electromagnetic storage and loss capabilities in this frequency range. In addition, the dielectric loss factor of MGO is much higher than the magnetic loss factor, and the dielectric loss is the main factor. The excellent dielectric loss performance is due to during the oxidation process, the carbon atoms of the microcrystalline graphite structural layer and the carbon atoms with chemical bonds broken at the edge combine with oxygen and oxygen-containing groups to form C–H and C–O–C, C–OH, –C=O, –COOH and other polar oxygen functional groups, which act as electric dipoles and provide polarization sources. The process of dipole polarization and relaxation occurs under the action of electromagnetic wave, which consumes the energy of electromagnetic wave. In Table 1, with the increase in the dosage of microcrystalline graphite, the total contents of C–H, C–O–C, –OH and C=O decreased from 79.19% (MGO-0.8) to 76.50% (MGO-1.6), resulting in a reduction in the polarization loss of intrinsic dipoles. It is worth noting that MGO-0.8 has more polar functional groups, but there is a dielectric mismatch problem and the dielectric loss performance is reduced. In addition, MGO have edge defects (Fig. 2b), which trap charge carriers and destroy charge balance, resulting in loss of defect polarization and consumption of electromagnetic wave energy. However, the defect density of the MGO increased with the increase of microcrystalline graphite dosage, which was contrary to the dielectric loss value. The reason may be that excessive defect polarization loss caused the impedance mismatch of the material, resulting in the decrease of dielectric loss.

To further analyze the dielectric loss mechanism of MGO samples, the Cole–Cole semicircle is used to analyze the dielectric loss form of MGO samples.[29] From Debye dipole relaxation, the relative complex dielectric constant can be expressed as eqn (6).[30] Where f is the frequency, τ is the relaxation time, and ε_s and ε_∞ are the fixed and optical permittivity respectively, the ε'–ε'' relationship can be obtained (eqn (9)).[9] Based on this mathematical equation it is concluded that the ε'–ε'' curve represents a single semicircle, usually defined as a Cole–Cole semicircle, each of which corresponds to a Debye relaxation process.

$$\varepsilon_r = \varepsilon_\infty + \frac{\varepsilon_s - \varepsilon_\infty}{1 + j2\pi f\tau} = \varepsilon'(f) + i\varepsilon''(f) \quad (6)$$

$$\varepsilon'(f) = \varepsilon_\infty + \frac{\varepsilon_s - \varepsilon_\infty}{1 + (2\pi f)^2\tau^2} \quad (7)$$

$$\varepsilon''(f) = \frac{2\pi f\tau(\varepsilon_s - \varepsilon_\infty)}{1 + (2\pi f)^2\tau^2} \quad (8)$$

$$(\varepsilon' - \varepsilon_\infty)^2 + (\varepsilon'')^2 = (\varepsilon_s - \varepsilon_\infty)^2 \quad (9)$$

Fig. 7 shows the Cole–Cole curve (Fig. 7a–e) and electrical conductance (Fig. 7f) of MGO. A perfect Debye relaxation model Cole–Cole curve should be a semi-circle, and the number and size of semi-circles can judge the strength and quantity of the material relaxation process. In Fig. 7, three semicircles appeared in the Cole–Cole curves of MGO samples, and the

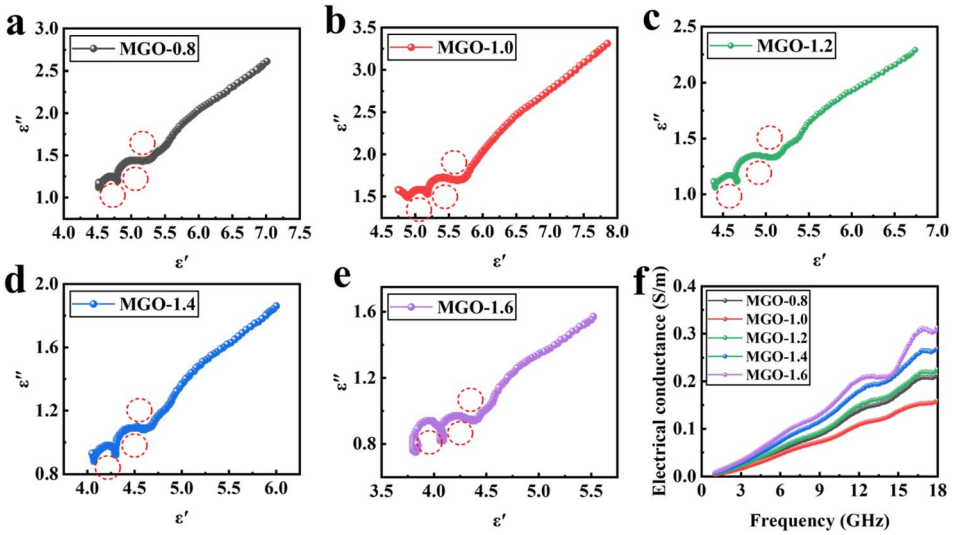

Fig. 7 Curves of complex permittivity real part (ε') – complex permittivity imaginary part (ε'') and electrical conductance of MGO (a–e – complex permittivity real part (ε') – complex permittivity imaginary part (ε''); f – electrical conductance).

diameter of the semicircles gradually decreased, and the relaxation loss intensity decreased. The reason is that the appearance of Cole–Cole semicircle is due to the dipole shift to polarization in the material, and with the increase of microcrystalline graphite addition, the MGO lamellar polarizing groups decrease, and the number of dipoles decreases as shown in Table 1, resulting in a gradual decrease in the diameter of the semicircle and a decrease in relaxation loss. In Fig. 7, the Cole–Cole curve of the MGO sample shows that the semicircle approaches a straight line and the ε'' has a high value, which indicates that there is a strong conductive loss in the MGO material.[31] In Fig. 7f, it is found that with the increase of microcrystalline graphite dosage, the conductivity of MGO increases gradually, which is opposite to the trend of conductivity loss. The reason may be due to the impedance mismatch caused by the high conductivity of MGO.

Impedance matching is an important parameter of absorption materials and is determined by the relationship between the complex permittivity and the complex permeability of the material. Impedance matching can be expressed in terms of modulus relative to the input impedance (eqn (10)).[32] The larger the attenuation constant value, the stronger the attenuation ability of electromagnetic wave. The attenuation constant can be expressed as eqn (11).[33] In addition, when the thickness of the absorption layer of the material satisfies the quarter-wavelength criterion, the reflected electromagnetic waves interfere and cancel at a suitable frequency. According to the quarter-wave resonance mechanism, the relationship between the matching thickness (t_m) and the peak frequency (f_m) can be related using eqn (12).[34]

$$Z = \left|\frac{Z_{in}}{Z_0}\right| = \sqrt{\frac{\mu_r}{\varepsilon_r}}\tanh\left[j\frac{2\pi f d}{c}\sqrt{\mu_r\varepsilon_r}\right] \quad (10)$$

$$\alpha = \frac{2\pi f d}{c}\sqrt{(\mu''\varepsilon'' - \mu'\varepsilon') + \sqrt{(\mu''\varepsilon'' - \mu'\varepsilon')^2 + (\mu''\varepsilon'' + \mu'\varepsilon')^2}} \quad (11)$$

$$t_m = \frac{n\lambda}{4} = \frac{nc}{4f_m\sqrt{|\mu_r||\varepsilon_r|}}(n = 1,\ 3,\ 5,\ \ldots) \quad (12)$$

Fig. 8 shows the RL, simulated thickness, impedance matching, and attenuation constant curves of the MGO. As shown in Fig. 8a–e, It can be observed that the RL_{min} peaks of MGO are shifted towards the lower frequencies as the matching thickness increases. This is due to the phase difference of 180°, which causes the electromagnetic wave to be dissipated at the air-absorber interface, thus bringing attenuation of microwave energy.[35] As we all know, impedance matching Z_{in} fluctuation in the range of 0.8–1.2 corresponds to the best electromagnetic wave absorption performance. When the microcrystalline graphite dosage is 1.0 g, the RL value of the sample is −18.39 dB, the impedance matching Z_{in} is 1.22, the attenuation constant α value appears a peak, and the electromagnetic wave attenuation ability is the strongest. In this case, there are intrinsic dipole polarization, defect polarization, and conductive loss. With the increase of the dosage of microcrystalline graphite, when the thickness of the absorbing layer is 3.6 mm, the impedance of the RL peak of the MGO sample first decreases and then increases. The impedance value of MGO-1.0 is the minimum of 1.22, which is closer to 1, and the absorbing energy is the best. It is worth noting that the impedances of MGO-0.8, MGO-1.2, MGO-1.4 and MGO-1.6 are 1.52, 1.63, 1.90 and 2.05 respectively, resulting in the problem of impedance mismatch. It is indicated that excessively high or low content of polar groups, electrical conductivity and defect density will all cause impedance mismatch problems, affecting the wave-

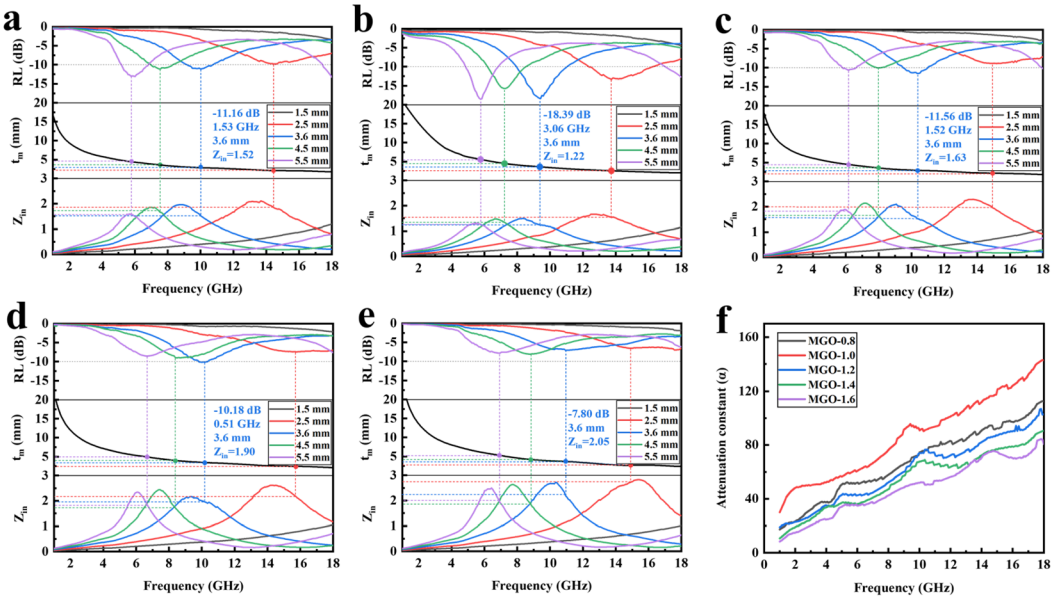

Fig. 8 Curves of RL, simulated thickness, impedance matching, and attenuation constant of MGO (a–e – curves of RL, simulated thickness, impedance matching; f – attenuation constant).

absorbing performance of the material. The attenuation capacity of MGO-1.0 is generally higher than that of other samples, and the attenuation capacity is the strongest.

In general, the MGO absorption materials were prepared by studying the dosage of microcrystalline graphite. The electromagnetic wave absorption performance is attributed to three points: 1. The carbon atoms in the microcrystalline graphite structure layer and the carbon atoms with chemical bond breaks at the edge combine with oxygen and oxygen-containing groups to form C–H and C–O–C, C–OH, –C═O, –COOH and other polar oxygen functional groups. These polar functional groups act as electric dipoles and provide polarization sources, and dipole polarization and relaxation processes occur under the action of electromagnetic wave, consuming electromagnetic energy. 2. Due to the low crystallinity of microcrystalline graphite, there are edge defects in the oxidation process, which will trap carriers and destroy the charge balance, resulting in the loss of defect polarization and the consumption of electromagnetic wave energy. 3. Graphite excellent layer conductive network, with high conductivity, their energy will be converted into electric current. During the transmission of electric current along electromagnetic wave absorbers, their instinct resistance will generate joule heat thus consuming electromagnetic wave energy.

4. Conclusions

In this study, microcrystalline graphene oxide (MGO) absorption materials were successfully prepared by the one-step oxidation method, and the electromagnetic wave absorption mechanism of MGO was clarified. When the dosage of microcrystalline graphite is 1.0 g, the overall layer number of the MGO samples are 1–2 layers, layer spacing is 0.900 nm, and the RL_{min} at the absorption layer thickness of 3.6 mm and the frequency of 9.42 GHz is −18.39 dB. And the EAB is 3.06 GHz (7.97–11.03 GHz). The feasibility of preparing microcrystalline graphene oxide absorbing materials by the Hummers method without adding sodium nitrate has been proved. The absorption properties of MGO are attributed to dipole polarization, defect polarization, and conductive loss. It is worth noting that the high conductivity, polar group, and edge defect density will cause the impedance mismatch of MGO and affect the microwave absorption properties. In addition, the main feature of MGO is dielectric loss, which has the limitation of a single-microwave absorption mechanism. Introducing it into the composite material strategy of magnetic materials will be a research hotspot of microcrystalline graphene oxide based MAMS in the future.

Data availability

The data from this study are all available and can provide raw data for editors and reviewers.

Author contributions

Conceptualization, Y. Z. and Z. M.; methodology, Y. Z., Z. M., X. W., and L. C.; validation, X. W., L. C., and Y. Q.; formal analysis, Y. Z., and Y. Q.; investigation, Z. M., and Y. Q.; resources, Z. M.; data curation, Y. Z.; writing – original draft preparation, Y. Z.; writing – review and editing, Y. Z.; visualization, Y. Q.; supervision, X. W., and L. C.; project administration, Z. M.; funding acquisition, Z. M. All authors have read and agreed to the published version of the manuscript.

Conflicts of interest

There are no conflicts to declare.

Acknowledgements

This work was supported by the National Natural Science Foundation of China [grant numbers 52274265].

Notes and references

1 M. Yu, Y. Huang, X. D. Liu, X. X. Zhao, W. Q. Fan and K. H. She, *Carbon*, 2023, **208**, 311–321.
2 T. Y. Chen, S. Jiang, L. L. Li, K. Qian, J. Sun, W. W. Guo, X. D. Cai and K. J. Yu, *Appl. Surf. Sci.*, 2022, **589**, 152858.
3 P. B. Li, G. Z. Zhang, H. X. Xu, S. C. Cheng, Y. Huang, O. Y. Bo, Y. T. Qian, R. X. Zhang and R. C. Che, *Adv. Funct. Mater.*, 2023, **33**(13), 2211298.
4 X. D. Liu, S. Zhang, M. Yu, X. X. Zhao, Y. W. Jia, Y. Huang and M. Zong, *Chem. Eng. J.*, 2023, **465**, 142932.
5 X. W. Jiang, H. H. Niu, J. L. Li, M. R. Li, C. Ma, R. Zhang, H. L. Wang, H. X. Lu, H. L. Xu and B. B. Fan, *Appl. Surf. Sci.*, 2023, **628**, 157355.
6 P. Wang, G. W. Wang, J. M. Zhang, B. F. Duan, L. H. Zheng, H. Zhang, D. L. He and T. Wang, *Chem. Eng. J.*, 2020, **382**, 122804.
7 J. Gao, Z. J. Ma, F. L. Liu, X. Y. Weng and K. Y. Meng, *Chem. Eng. J.*, 2022, **446**, 137157.
8 C. Liu, J. P. Lin, N. Wu, C. X. Weng, M. R. Han, W. Liu, J. R. Liu and Z. H. Zeng, *Carbon*, 2024, **223**, 119017.
9 X. K. Pang, X. H. Zhou, Y. Gao, Y. F. Qian and L. H. Lyu, *Polym. Compos.*, 2024, **45**(9), 8414–8425.
10 W. D. Xu, R. Q. Wang and P. Chen, *Chin. J. Mater. Res.*, 2024, **38**(01), 1–13.
11 Z. J. Ma, C. Y. Mang and Y. S. Zheng, *Non-Met. Mines*, 2018, **41**(04), 59–61.
12 W. Xie, W. Tang and J. C. Kuang, *New Chem. Mater.*, 2014, **42**(10), 131–133.
13 W. Xie, J. C. Kuang and H. F. Cheng, *Mater. Rep.*, 2013, **27**(20), 67–70.
14 S. Suman, C. Tanmoy, S. Aliva, D. Solanky, P. Goutam, K. P. Anup, C. Chanchal, D. Sukhen and S. Soumyaditya, *Carbon*, 2024, **220**, 118829.
15 G. M. Wang, Z. J. Ma, Y. S. Zheng, L. Cheng, H. L. Xing and Z. M. Li, *RSC Adv.*, 2024, **14**, 38345.

16 F. T. Johra, J. W. Lee and W. G. Jung, *J. Ind. Eng. Chem.*, 2014, **20**(5), 2883–2887.
17 A. N. Popova, *Coke Chem.*, 2017, **60**, 361–365.
18 J. Gao, Z. J. Ma, F. L. Liu, X. Y. Weng and K. Y. Meng, *Chem. Eng. J.*, 2022, **44**, 137157.
19 L. Karnis, F. Krasanakis, L. Sygellou, A. N. Rissanou, K. Karatasos and K. Chrissopoulou, *Phys. Chem. Chem. Phys.*, 2024, **26**, 10054.
20 J. X. Wu, H. Xu and J. Zhang, *Acta Chim. Sin.*, 2014, **72**(03), 301–318.
21 B. Li, L. Zhou, D. Wu, H. L. Peng, K. Yan, Y. Zhou and Z. F. Liu, *ACS Nano*, 2011, **5**(7), 5957–5961.
22 A. Eckmann, A. Felten, A. Mishchenko, L. Britnell, R. Krupke, K. S. Novoselov and C. Casiraghi, *Nano Lett.*, 2012, **12**(8), 3925–3930.
23 J. F. Chen, M. Duan and G. H. Chen, *J. Mater. Chem.*, 2012, **22**(37), 19625–19628.
24 S. B. Narang and K. Pubby, *J. Magn. Magn. Mater.*, 2021, **519**, 167163.
25 K. Pubby, S. S. Meena, S. M. Yusuf and S. B. Narang, *J. Magn. Magn. Mater.*, 2018, **466**, 430–445.
26 Z. N. Xiang, Q. C. He, Y. Q. Wang, X. M. Yin and B. K. Xu, *Appl. Surf. Sci.*, 2022, **599**, 153968.
27 X. J. Zeng, X. Y. Cheng, R. H. Yu and G. D. Stucky, *Carbon*, 2020, **168**, 606–623.
28 X. J. Zhang, S. Li, S. W. Wang, Z. J. Yin, J. Q. Zhu, A. P. Guo, G. S. Wang, P. G. Yin and L. Guo, *J. Phys. Chem. C*, 2016, **120**, 22019–22027.
29 X. C. Di, Y. Wang, Z. Lu, R. R. Cheng, L. Q. Yang and X. M. Wu, *Carbon*, 2021, **179**, 565–578.
30 J. Frenkel and J. Doefman, *Nature*, 1930, **126**, 274–275.
31 R. Yu, H. Zhang and B. Guo, *Nano-Micro Lett.*, 2022, **14**, 1.
32 W. Liu, L. Liu, G. B. Ji, D. R. Li, Y. N. Zhang, J. N. Ma and Y. W. Du, *ACS Sustainable Chem. Eng.*, 2017, **5**(9), 7961–7971.
33 Y. Qiu, H. B. Yang, Y. Cheng, B. Wen and Y. Lin, *Appl. Surf. Sci.*, 2022, **571**, 151334.
34 Z. X. Li, X. H. Li, Y. Zong, G. G. Tan, Y. Sun, Y. Y. Lan, M. He, Z. Y. Ren and X. L. Zheng, *Carbon*, 2017, **115**, 493–502.
35 L. Lei, Z. J. Yao, J. T. Zhou, W. J. Zheng, B. Wei, J. Q. Zu and K. Y. Yan, *Carbon*, 2021, **173**, 69–79.